

THE IMPACT OF HYDRATE SATURATION ON THE MECHANICAL, ELECTRICAL, AND THERMAL PROPERTIES OF HYDRATE-BEARING SAND, SILTS, AND CLAY

J. Carlos Santamarina*
School of Civil and Environmental Engineering
Georgia Institute of Technology
790 Atlantic Dr., NW, Atlanta, GA 30332-0355

Carolyn Ruppel
U.S. Geological Survey
384 Woods Hole Road, Woods Hole, MA 02543

ABSTRACT

An understanding of the physical properties of hydrate-bearing sediments is important for interpretation of geophysical data collected in field settings, borehole and slope stability analyses, and reservoir simulation and production models. Yet current knowledge of geophysical and geotechnical properties of hydrate-bearing sediments is still largely derived from laboratory experiments conducted on disparate soils at different confining pressures, degrees of water saturation, and hydrate concentrations. Here we report on the key findings that have emerged from 5 years of laboratory experiments conducted on synthetic samples of sand, silts, or clays subjected to various confining pressures in standardized geotechnical laboratory devices and containing carefully controlled saturations of tetrahydrofuran hydrate formed from the dissolved phase. For the first time, we use this internally-consistent data set to conduct a comprehensive analysis of the trends in geophysical and geotechnical properties as a function of hydrate saturation, soil characteristics, and other parameters. Our experiments emphasize measurements of seismic velocities, electrical conductivity and permittivity, large strain deformation and strength, and thermal conductivity. We discuss the impact of hydrate formation technique on the resulting physical properties measurements and use our data set to identify systematic effects of sediment characteristics, hydrate concentration, and state of stress, extracting robust relationships (often based on micromechanical concepts) for the most relevant material parameters. The mathematical trends that emerge for the measured physical parameters always require that the hydrate saturation in pore space, which ranges from 0 to 1, be raised to a power greater than 1. This significantly reduces the impact of low hydrate saturations on the measured physical parameters, an effect that is particularly pronounced at the hydrate saturations characteristic of many natural systems (<0.2 of pore space). The results also reveal that the electrical properties of hydrate-bearing sediments are less sensitive to the method used to form hydrate in the lab (which controls the pore-scale arrangement of hydrate and sediment grains) than to hydrate saturation. Mechanical properties are strongly influenced by both soil properties and the hydrate loci. Thermal conductivity depends on the complex interplay of a variety of factors, including formation history, and cannot be easily predicted by volume average formulations.

Keywords: gas hydrates, physical properties, seismic velocity, conductivity, permittivity, strength, thermal conductivity, formation mechanism

* Corresponding author: Phone: 404 894 0231 Fax: 404 894 2281 E-mail: jcs@gatech.edu

NOMENCLATURE

a	Coefficient in strength expression (4)
b	Coefficient in strength expression (4)
B	Bulk stiffness [MPa]
C_c	Compression coefficient []
C_{ex}	Expansion coefficient []
D_{50}	Mean grain size [μm]; 50% of sample by mass is smaller than D_{50}
E_{50}	Secant longitudinal stiffness at half the failure strength [MPa]
e_{max}	Maximum packing void ratio []
e_{min}	Minimum packing void ratio []
f	Exponent in Figure 9
h	Subscript denoting pure hydrate
hbs	Subscript denoting hydrate-bearing sediment
k_0	Effective stress ratio at rest []
K	Thermal conductivity [$\text{Wm}^{-1}\text{K}^{-1}$]
m	Subscript denoting mineral grains
n	Porosity []
q_h	Strength of pure hydrate [MPa]
s	Exponent, thermal conductivity eq. (10) []
S_h	Hydrate saturation in pore space []; $0 \leq S_h \leq 1$, corresponding to 0% to 100% of pore space
S_u	Peak undrained shear strength [MPa]
ΔV	Volume change for phase transformation [m^3]
V_{hbs}	Shear wave velocity for hydrate-bearing sediments [m/s]
V_p	Compressional wave velocity [m/s]
V_s	Shear wave velocity [m/s]
w	Subscript denoting liquid in the pore fluid
α	Shear wave velocity at 1 kPa [m/s]
β	Coefficient representing sensitivity of shear wave velocity to state of stress in (1) and (2)
δ	Coefficient in Archie relationship (7)
ε	Strain []
θ	Coefficient [] in shear wave velocity expression (2)
κ'	Relative permittivity []
λ	Porosity exponent, Archie relationship (7) []
ν_{sk}	Small-strain Poisson ratio for soil skeleton []
σ'	Effective stress [MPa] (always primed)
σ'_{\parallel}	Stress in direction of propagation [MPa]
σ'_{\perp}	Stress in direction of particle motion [MPa]
σ'_d	Deviatoric stress [MPa]
σ'_o	Isotropic effective stress [MPa]
σ'_h	Effective horizontal stress [MPa]
σ'_z	Applied vertical effective stress [MPa]
σ	Electrical conductivity [S/m]
χ	Exponent in Archie relation

INTRODUCTION

Numerous published studies report on laboratory measurements of the geophysical and geotechnical properties of hydrate-bearing sediments, but many fundamental challenges remain in using this information to interpret borehole logs or other field data obtained in hydrate provinces. For example, most studies report on only a small subset of physical properties, and the experimental conditions adopted for various studies of the same physical property can be so different as to render the comparison of results impossible. The difficulty of maintaining hydrate-bearing sediments within the hydrate stability field has led some researchers to construct specialized devices for their experiments, reducing the potential for reproducing results in other laboratories under exactly the same set of experimental conditions.

Starting in 2002, we undertook an exhaustive series of laboratory measurements to determine the large-strain and small-strain mechanical properties, thermal properties, and electrical/electromagnetic properties of hydrate-bearing soils using standardized geotechnical devices and test protocols (Table 1). With sponsorship from the Chevron Joint Industry Project (JIP) on Methane Hydrates through the U.S. Department of Energy, we conducted experiments on soils with a range of grain sizes subject to effective stress up to 2 MPa and with well-controlled saturations of synthetic hydrate [1]. The goal of this research was to provide an internally-consistent, systematically-acquired database that could assist in reservoir assessment, geomechanical analyses, hazards evaluation (e.g., borehole stability models of [2]), and development of production methodologies, covering both the sandy lithologies and fine-grained sediments anticipated during drilling of the northern Gulf of Mexico gas hydrate province by the Chevron JIP ([3-5]). This manuscript starts with a general discussion of the methodology, followed by a presentation of the results and summary trends that can be extracted from the data. We focus only on our own data. Comparisons with other data sets are provided in the associated papers, theses, and related documents cited in this paper [6-10].

S_h	Effective Stress (MPa)	σ'_z vs. ϵ_z	E_{50} (MPa)	S_u (MPa)	σ'_z vs. ϵ_z	C_c	ΔV (m ³)	C_{ex}	V_p (m/s)	V_s (m/s)	σ (S/m)	κ'	K (Wm ⁻¹ K ⁻¹)
0	0.01	T	T	T	O	O	O	O	O	O, C	O	O	I
	0.50	T	T	T	O	O	O	O	O	O, C	O	O	I
	1.00	T	T	T	O	O	O	O	O	O, C	O	O	I
	2.00								O	C	O		
0.5	0.01	T	T	T	O	O	O	O	O	O, C	O	O	I
	0.50	T	T	T	O	O	O	O	O	O, C	O	O	I
	1.00	T	T	T	O	O	O	O	O	O, C	O	O	I
	2.00								O	C	O		
1.0	0.01	T	T	T	O	O	O	O	O	O, C	O	O	I
	0.50	T	T	T	O	O	O	O	O	O, C	O	O	I
	1.00	T	T	T	O	O	O	O	O	O, C	O	O	I
	2.00								O	C	O		

Table 1. Hydrate saturations (S_h) and effective stress states for the parameters directly measured (see nomenclature) in the laboratory experiments using a triaxial device (T), oedometer cell (O), high pressure cell (C), and isotropic cell (I). This matrix of tests was run for the sand, precipitated silt, and kaolinite sediments. For crushed silt, we ran the indicated tests with $S_h=0$ and $S_h=1$ only.

METHODS

Soils

We tested four soils (sand, crushed silt, precipitated silt, and kaolinite) to cover the range of grain size, specific surface, and mineralogy in lithologies present in natural hydrate-bearing systems. The characteristics of these soils are summarized in Table 2. The soils have D_{50} ranging from 1.1 μm (kaolinite) to 120 μm (sand) and specific surface of 0.019 $\text{m}^2 \text{g}^{-1}$ (sand) to 120 $\text{m}^2 \text{g}^{-1}$ (precipitated silt). Figure 1 shows the tested soils.

Despite the same D_{50} values for precipitated and crushed silt, the specific surface of precipitated silt is 3 orders of magnitude greater than that of crushed silt. Similar to diatoms, precipitated silt is a dual porosity medium having internal porosity. The dual porosity characteristic alters the pore-scale properties of the samples formed from precipitated silt. Considering grain and pore size differences, many physical properties we describe in this paper are expected to reveal an ordering of clay-silt-sand. As will be shown below, the properties we measure are in some cases more strongly dependent on specific surface, and thus the properties of the specimens containing precipitated silt do not always follow the expected ordering.

Fitting global trends to the data we acquired on precipitated silt specimens has sometimes proved difficult. Yet this type of soil merits inclusion in the analysis and further future study owing to the common occurrence of dual porosity materials in natural sediments.

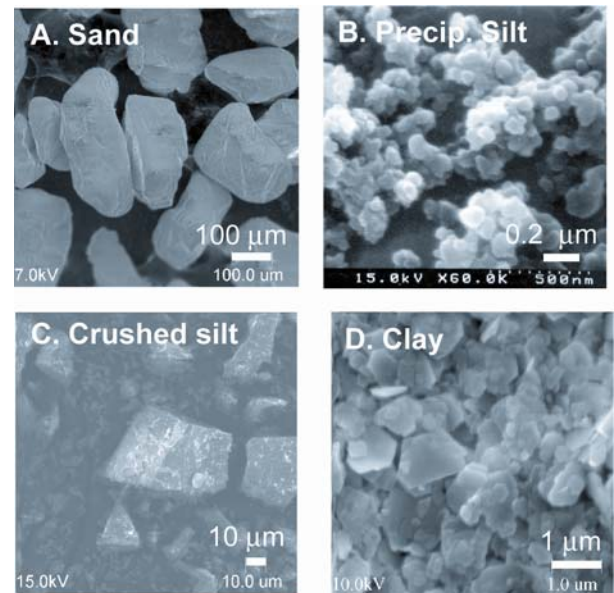


Figure 1. Photomicrographs of the four soil types used for experiments. Soil characteristics are summarized in Table 2 and [6].

Soil	Figure number	D ₅₀ (μm)	Specific Gravity	Specific Surface (m ² g ⁻¹)	e _{min}	e _{max}	Sphericity	Roundness
Sand (F110)	1A	120	2.65	0.019	0.54	0.85	0.7	0.7
Precipitated silt (Silica zeofree 5161)	1B	20	2.2	120	---	---	0.9	0.7
Crushed silt (Sil Co Sil 106)	1C	20	2.65	0.113	0.7	1.51	0.9	0.1
Kaolinite (SA1)	1D	1.1	2.6	36	---	---	0.7	0.1

Table 2. Properties of soils used for preparing hydrate-bearing specimens. Values of e_{min} and e_{max} apply only to coarse-grained soils.

Hydrate Formation and Hydrate Former

As noted above, numerous published studies on the laboratory physical properties of hydrate-bearing sediments have produced results that are sometimes difficult to compare to the properties measured by or inferred from real field data. A key problem is the role that the experimental method for hydrate formation in the laboratory plays in controlling the resulting physical properties. In nature, much of the methane hydrate in marine settings probably forms from methane in the dissolved phase [11], but laboratory techniques that efficiently and consistently produce methane hydrate in porous samples at controllable saturations are still in their infancy [12, 13] and cannot be routinely applied for the measurement of suites of physical properties for a range of fine-grained to coarse-grained hydrate-bearing soils [8]. Other methods of forming methane hydrate—from ice seeds [14, 15] or from unsaturated conditions (e.g., Ref. [16])—a priori control where the hydrate will nucleate in porous samples and therefore systematically bias some physical parameters, particularly mechanical properties [6, 8, 9].

Figure 2 provides an illustrative example of the impact of laboratory hydrate formation techniques on measured compressional and shear wave velocities of hydrate-bearing sediments. Although differences among the soil types and other parameters in these experiments render exact comparison of results difficult, the trends in Figure 2 show that hydrate formed from unsaturated conditions (including the ice-seed method) increases skeletal stiffness at lower hydrate

saturations, which reflects preferential hydrate formation at menisci between grains and early cementation of grains. Hydrate formed from the dissolved phase does not increase skeletal stiffness significantly until hydrate saturation exceeds ~0.4 (e.g., Refs. [6, 7, 17]). Despite the difficulty of drawing an exact comparison, the general trends highlighted here underscore the need to carefully consider the formation history in the interpretation of properties gathered for synthetic hydrate-bearing sediments.

We adopted tetrahydrofuran (THF) as the hydrate former for this study. A full discussion of the nature of the THF molecule relative to methane, the phase diagram for THF hydrate, and experimental issues related to the use of THF hydrate for studies of the physical properties of hydrate-bearing porous media is given in [8]. A major conclusion of Ref. [8] is that THF, a Structure II hydrate former, is an appropriate proxy for methane hydrate, a Structure I former, particularly for experiments measuring the mechanical properties of hydrate-bearing sediments. THF has important advantages over methane though, including complete miscibility with water. This makes it possible to form THF hydrate from the dissolved phase and to control the final saturation of hydrate (S_h) in the sample through the choice of the appropriate initial water-THF combination used to saturate the soil.

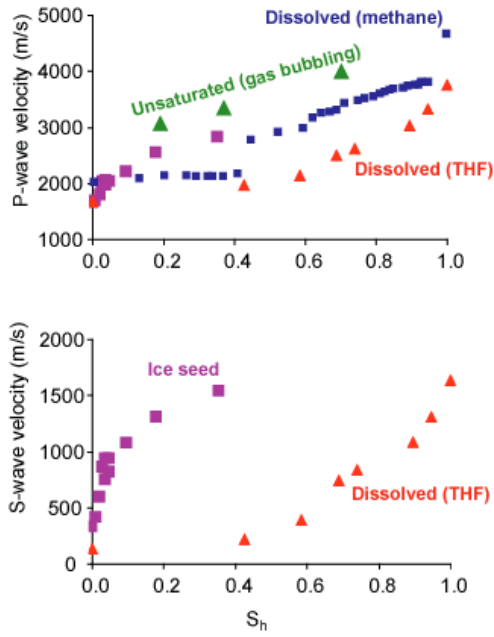


Figure 2. Comparison of P-wave (top) and S-wave (bottom) velocities measured on hydrate-bearing sands as a function of S_h for different methods of forming hydrate in the laboratory. Red triangles denote data for THF hydrate formed from dissolved phase [7]. Blue squares are measurements by [12] for hydrate formation from dissolved phase methane. The ice seed results are from [15], and unsaturated data were reported by [16]. Different sands were used for each experiment, and other experimental conditions also varied. Ref. [7] discusses the morphology of these curves with respect to pore filling vs. cementation modes of hydrate formation, and [9] provides greater detail about the role of hydrate formation method on measured V_p and V_s .

For our experiments, endmember hydrate saturations were attained using water alone ($S_h=0$) or the appropriate stoichiometric solution of 81% water combined with 19% THF by mass for $S_h=1$ (100% of pore space). For the case of $S_h=0.5$ (50% of pore space), we used excess water (9% THF and 91% water initial solution) for some properties and excess THF (57% THF and 43% water initial solution) for others. Excess THF is preferred to avoid ice formation, a problem in excess water experiments. However, excess water must be used for the appropriate measurement of electrical properties in hydrate-bearing sediments. Further discussion of stoichiometric mixtures with respect to the THF hydrate phase diagram and of the challenges associated with using THF (e.g.,

overcoming problems related to evaporation) can be found in [6] and [8].

Laboratory Cells and Test Devices

The porosity, skeletal stiffness, strength, and dilative tendency of sediments are controlled by the state of effective stress. Therefore, sediments for our laboratory experiments are confined in cells that allow the application of effective stresses. Three boundary conditions are simulated: (1) For thermal conductivity measurements, we adapt an axisymmetric cell and apply an isotropic state of effective stress. The specimen is held within a latex membrane, and the external confinement pressure is applied with oil. Hydrate is formed within the insulated cell once the isotropic state of effective stress is reached in the soil sample. (2) A zero-lateral strain loading condition is used to study sediment stiffness on loading, volume change during dissociation, and electromagnetic and elastic wave propagation. We use two oedometers for this work. For the first, the steady state fluid pressure is atmospheric pressure; the other has been adapted to allow us to control fluid pressure up to 20 MPa. During loading, the state of effective stress in the specimen is the applied vertical stress σ'_z and the ensuing effective horizontal stress is $\sigma'_x = k_0 \sigma'_z$, where k_0 is the effective stress ratio at rest. Hydrate is formed after the desired vertical effective stress is reached, i.e., after any excess pore pressure caused during loading has dissipated. (3) The triaxial test configuration is used for the determination of Coulomb strength parameters. The cylindrical specimen is held in a latex membrane between two metal endcaps. The test starts with the application of the desired isotropic effective stress σ'_o , and hydrate is formed at this point. The deviatoric load σ'_d is then applied on the hydrate-bearing sediment until failure is reached.

RESULTS AND INTERPRETATIONS

In the following sections, we place emphasis on identifying robust trends in the global data sets, as a function of soil type, soil parameters, and/or hydrate saturation. Instead of providing merely empirical functional fits (e.g., linear, log, quadratic) to the data and associated coefficients, we focus on producing mathematical relationships among key parameters to provide physical insight

into the mechanistic processes controlling the observations.

Small strain stiffness

The shear wave velocity for all soils without hydrates satisfies a power equation of the effective stresses acting in the direction of wave propagation (subscript \parallel) and particle motion (subscript \perp):

$$V_s = \alpha \left(\frac{\sigma'_{\parallel} + \sigma'_{\perp}}{2 \text{ kPa}} \right)^{\beta}, \quad (1)$$

where α is the shear wave velocity at 1 kPa and the exponent β captures the sensitivity of the velocity to the state of stress. In all sediments, β is inversely related to α .

The shear wave velocity in hydrate-bearing sediments is stress dependent at low hydrate concentration, but it becomes hydrate controlled at high hydrate concentration. When the data for all soils and stress levels are plotted against hydrate concentration, the trend shows a minor increase up to $S_h=0.5$ and major increase as the hydrate concentration approaches $S_h=1$, following the parabolic trend described by [7]. On the other hand, the lower the porosity is, the higher the stiffness in the hydrate-bearing sediment. In other words, hydrate is more effective in contributing to the global sediment stiffness for lower porosity sediments. Following these data-based observations, and adopting the form of theoretical expressions for cemented soils [18], we fit the data with:

$$V_{hbs} = \sqrt[2]{\left(\frac{V_h S_h^2}{n} \right)^2 \theta + \left[\alpha \left(\frac{\sigma'_{\parallel} + \sigma'_{\perp}}{2 \text{ kPa}} \right)^{\beta} \right]^2}, \quad (2)$$

where the factor θ captures the hydrate habit in the pore space, and α and β can be extracted from tests conducted on sediment without hydrates ($S_h=0$). Measured and predicted values for all sediments, hydrate content, and effective stress levels are plotted in Figure 3.

When hydrate forms in unsaturated specimens, we expect θ to be larger than for our experiments

owing to the preferred loci for hydrate nucleation at interparticle contacts (menisci).

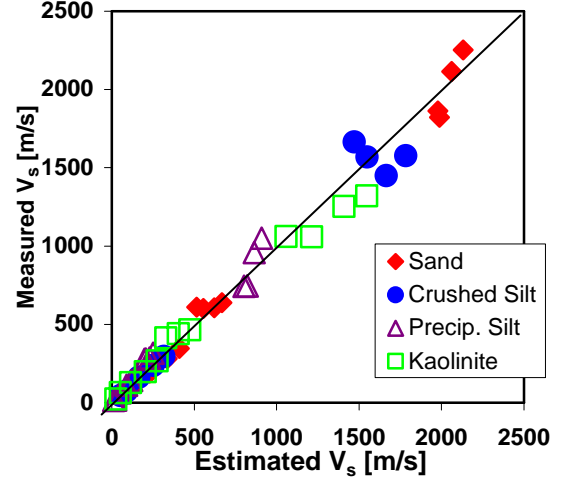


Figure 3. Measured versus estimated shear wave velocities for all soils, S_h and effective stress levels. Fitting parameters are sand ($\alpha=80$ m/s, $\beta=0.25$, $\theta=0.15$), crushed silt ($\alpha=50$ m/s, $\beta=0.26$, $\theta=0.12$), precipitated silt ($\alpha=10$ m/s, $\beta=0.35$, $\theta=0.13$), and kaolinite ($\alpha=23$ m/s, $\beta=0.35$, $\theta=0.07$).

The P-wave velocity V_p in hydrate-bearing sediments can be computed from the shear wave velocity of the hydrate-bearing sediment V_{hbs} , and the volume fraction and bulk stiffness B of the component phases. Following a Biot-Gassmann type formulation (see [19]) for low skeletal stiffness $B_{sk}/B_w \ll 1$,

$$V_p^2 = V_{hbs}^2 \left(\frac{1 - \nu_{sk}}{1 - 2\nu_{sk}} + \frac{4}{3} \right) + \frac{1}{\rho_{mix}} \left(\frac{1-n}{B_m} + n \left(\frac{S_h}{B_h} + \frac{1-S_h}{B_w} \right) \right)^{-1}. \quad (3)$$

Note that the small strain Poisson's ratio for the skeleton ν_{sk} is typically 0.1 ± 0.05 [19].

High strain stiffness and strength

Effective stress data for low hydrate concentration sediments (i.e., $S_h < 0.5$) show an increase in dilative tendency proportional to the hydrate volume fraction S_h , very low or no cohesion

intercept, and critical state friction angle similar to the sediment without hydrate [20].

Our data place emphasis on high hydrate concentration sediments ($S_h \geq 0.5$). Due to the diminished hydraulic conductivity in these circumstances, we impose the deviatoric stress σ'_d under undrained conditions and report the total stress undrained response herein. The deviatoric stress vs. strain response (σ'_d vs. ε) is characterized by increased secant stiffness, undrained strength, and brittleness with increasing hydrate concentration [6].

The general analysis of the strength data leads to the following observations: (1) The undrained shear strength at low hydrate concentration is determined by the effective stress-dependent frictional strength; (2) the contribution of the hydrate strength increases nonlinearly with higher strength, gaining relevance at high S_h ; (3) in the case of fine grained soils, the effect of hydrate tends to be more pronounced at low porosity—changes in porosity with effective confinement are very minor in coarse-grained sediments. The following expression for S_u captures these observations:

$$S_u = a\sigma'_o + bq_h \left(\frac{S_h}{n} \right)^2, \quad (4)$$

where a nominal value for the hydrate strength $q_h = 8$ MPa is assumed. This value is within the range reported in the literature [21]. The coefficient a captures friction and pore pressure generation in the sediment, while b is an indication of the hydrate's ability to contribute to the strength of the hydrate-bearing sediment. In other words, b is expected to reflect the formation method/habit of hydrate in a given soil. Measured and predicted values for all sediments, hydrate content, and effective stress level are plotted in Figure 4.

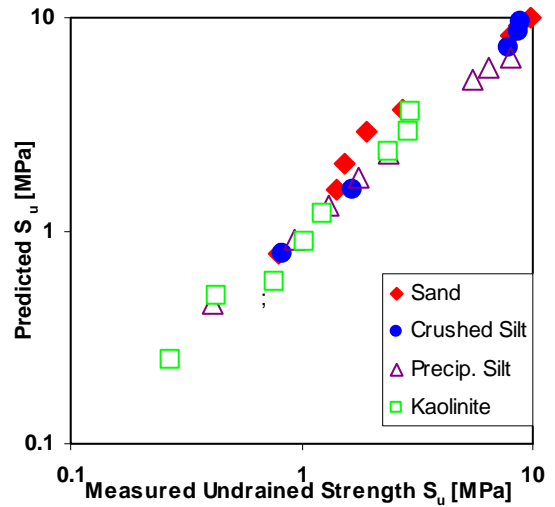


Figure 4. Measured versus estimated undrained shear strength S_u for all soils, S_h and effective stress levels. Fitting parameters are sand ($a=1.55$, $b=0.14$), crushed silt ($a=1.55$, $b=0.16$), precipitated silt ($a=0.9$, $b=0.5$), and kaolinite ($a=0.5$, $b=0.07$).

As in most materials, there is proportionality between the longitudinal stiffness half way to failure (secant stiffness) E_{50} and the peak strength S_u , as shown in Figure 5. A simple linear expression can be used [6]:

$$E_{50} \approx 100 S_u \quad (5)$$

It should be noted that the data display significant deviations from this trend. For example, the coefficient in (6) for kaolinite specimens exceeds 300 for $S_h=0.5$ or 1. Therefore, the expression should only be used for preliminary analyses. More details about the determination of secant stiffness and an extensive analysis of the laboratory strength and stress-strain results are given in [6].

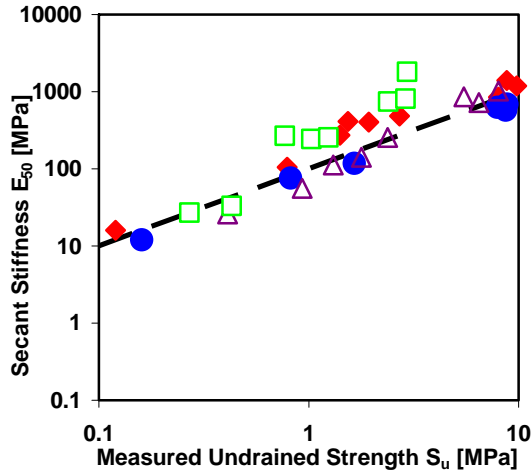


Figure 5: Proportionality between secant stiffness E_{50} and peak strength. Data are for all soils, with and without hydrates, and at all effective stresses. Dashed line is equation (5), and the symbols are the same as in Figure 4.

Electrical conductivity

The electrical conductivity of hydrate-bearing sediments σ_{hbs} at radiofrequencies is determined by the volume fraction of the unfrozen pore fluid and the pore fluid conductivity so that $\sigma_{hbs} \approx \sigma_w n(1-S_h)$. Our data show a decrease in electrical conductivity associated with lower porosity and increased hydrate formation [9], but also reflect the special role that specific surface plays in affecting conduction.

In general, laboratory and field data are properly predicted by adding fitting parameters to the previous expression in the form of Archie's law, $\sigma_{hbs} = \delta \sigma_w n^\lambda (1-S_h)^\chi$. Reported values for hydrate-bearing sediments are $\delta=1\pm0.35$, $\lambda=2.2\pm0.5$, and $\chi=1.9\pm0.15$ (e.g., [22, 23]). While parameters in Archie-type expressions can be readily used to closely match any given dataset, we seek to identify a robust expression that can approximate the data for all soils, hydrate concentrations, and effective stresses simultaneously. The resulting expression is:

$$\sigma_{hbs} = \sigma_w [n(1-S_h)]^{1.6}, \quad (7)$$

which corresponds to Archie's parameters $\delta=1$ and $\lambda=\chi=1.6$. As observed with other parameters, the

data for the dual porosity precipitated silt at $S_h=0.5$ deviates most sharply from this trend (Figure 6).

Note that the fitting parameters in the Archie relationship account for fabric, surface conduction, and other particle-scale electrical processes discussed above. Together with our laboratory results, this observation about the fitting parameters highlights the importance of being cautious in applying Archie-type expressions to monitor pore water freshening during hydrate dissociation in clayey sediments.

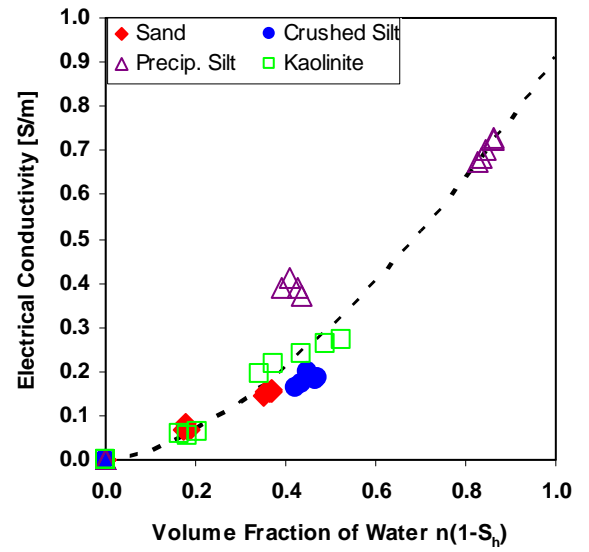


Figure 6. Measured electrical conductivity for all soils, S_h , and effective stress levels. The reference line shown corresponds to equation (6).

Permittivity

The electrical permittivity in the microwave frequency range is determined by the polarization of the free, unfrozen water; therefore, the permittivity of hydrate-bearing sediments κ'_{hbs} is proportional to $n(1-S_h)\kappa'_w$. This is readily observed in our experimental results (Figure 7 and [9]). Except for the data for precipitated silt (a dual porosity medium) at $S_h=0.5$, all other data tend to plot near or below the volume average line given by:

$$\kappa'_{hbs} = 5 + 70 \cdot n(1-S_h) \quad (8)$$

A more predictive expression is based on the CRIM-type model,

$$\begin{aligned}
\sqrt{\kappa'_{hbs}} &= (1-n)\sqrt{\kappa'_m} + n(S_h\sqrt{\kappa'_h} + S_w\sqrt{\kappa'_w}) \\
&= (1-n)\sqrt{\kappa'_m} + nS_h\sqrt{\kappa'_h} + n(1-S_h)\sqrt{\kappa'_w} \quad (9) \\
&\approx 2.8 + 6n - 7nS_h
\end{aligned}$$

The last approximation is obtained by fitting the expression to all the data, while adequately satisfying the extreme conditions for pure mineral ($n=0$), pure water ($n=1$ and $S_h=0$), and pure hydrate ($n=1$ and $S_h=1$).

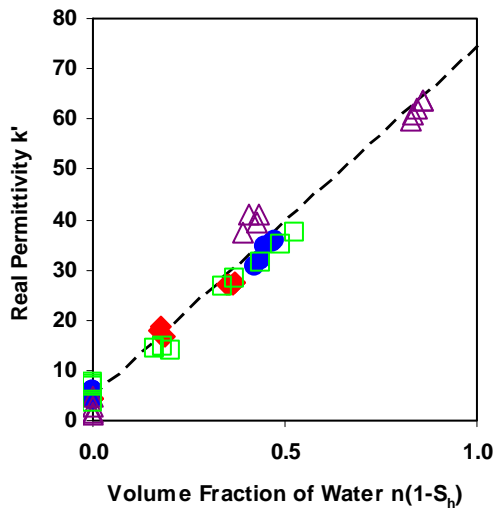


Figure 7. Measured real permittivity (at 1 GHz) for all soils, S_h , and effective stress levels. The reference line is the linear volume average of equation (7). Symbols are the same as in Figure 6.

Thermal conductivity

The thermal conductivity was determined using the needle probe technique in sediments subjected to isotropic confinement [10]. An overview of the data is presented in Figure 8. The data show that the thermal conductivity increases with decreasing porosity in soils without hydrates. The general Pythagorean mixing formula applies:

$$K_{hbs} = \left[n(S_h K_h^s + S_w K_w^s) + (1-n) \cdot K_m^s \right]^{1/s} \quad (10)$$

Note that this expression can be readily extended to include ice and gas phases in cases when these phases may be present. The parallel model corresponds to $s=1$ in (10) and the series model to $s=-1$. Adequate predictions for a given soil are obtained with exponents in the $s \approx \pm 0.2$ range. The

two trends superimposed on Figure 8 were computed assuming that the pore fluid is either cold water or a water-THF solution, so that an intermediate $K_w=0.5 \text{ Wm}^{-1}\text{K}^{-1}$ value is selected. The upper trend shown as a gray line corresponds to sandy soils ($K_m=8 \text{ Wm}^{-1}\text{K}^{-1}$, $s=0.1$), and the lower black line applies to fine-grained kaolinite and precipitated silica ($K_m=5 \text{ Wm}^{-1}\text{K}^{-1}$, $s=0.2$).

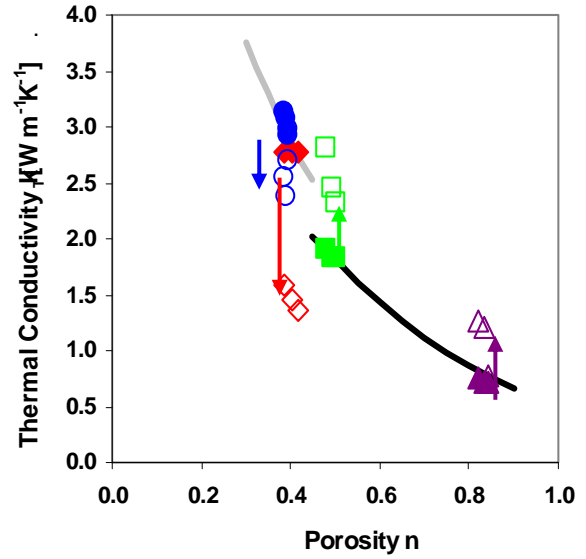


Figure 8. Measured thermal conductivity for all soils and effective stress levels, for $S_h=0$ (solid symbols) and 1 (open symbols). Color coding is red for sand, blue for crushed silt, purple for precipitated silt, and green for kaolinite. The color-coded arrows show how thermal conductivity changes between the hydrate-free and hydrate-bearing soils. The two trends (black and gray curves) were computed with Equation (10), using the parameters given in the text.

While the thermal conductivity of hydrate is very similar to that of water, there are marked changes in thermal conductivity when hydrates form to high S_h in soils. Complex underlying particle-level processes are inferred based on trends in Figure 8. In particular, the reduction in thermal conductivity hydrate-free and hydrate-bearing sands and crushed silt may reflect grain separation due to volume expansion during the hydrate formation. On the other hand, the increase in thermal conductivity between hydrate-free and hydrate-bearing fine-grained precipitated silica and kaolinite may be a consequence of cryogenic

suction and the formation of lenses. Such hypotheses are discussed in more detail in a forthcoming manuscript.

CONCLUDING REMARKS

In this paper, we report in concise form on the exhaustive physical properties data set we collected on THF hydrate-bearing clay, silt (precipitated and crushed), and sand using standardized geotechnical devices and test protocols. Within the scope of this manuscript, we do not compare our results to those of other workers, apart from emphasizing that careful consideration must be given to the method adopted for formation of hydrate in the laboratory. Particularly for mechanical measurements, different hydrate formation techniques (e.g., from dissolved phase, ice seeds, or gas bubbles) produce predictably different properties that reflect the loci of hydrate nucleation and growth (e.g., [6, 7]).

Throughout this analysis, we have emphasized the determination of data trends using physically-based mathematical relationships that combine material parameters, instead of merely fitting generic mathematical functions to the data. A key observation is that S_h , which can range from 0 to 1, is raised to a power greater than 1 in all of the expressions reported here. Mathematically, this means that the impact of hydrate on physical properties is greatly reduced in sediments having low S_h values. Figure 9 illustrates how raising S_h to powers ranging from 1 to 3 more strongly reduces the impact of low S_h values in the resulting expressions for physical property trends. The impact of the exponential terms is particularly striking for $0 < S_h < 0.2$, a common S_h range in many natural hydrate systems.

The power-law trends that have emerged from our laboratory data imply that higher values of S_h are needed to produce a marked effect on measured properties of hydrate-bearing sediments. These trends also provide a natural explanation for the difficulty often encountered in assessing sediments with low S_h using geophysical data or borehole logs in field settings. Taken together, these observations support the need for more laboratory research on the properties of hydrate-bearing sediments with $S_h=0$ to 0.5, a range of saturations that our data set samples only at the endmembers. Future laboratory programs should pay close attention to (a) the detailed characteristics of the

soils chosen for the experiments and (b) the impact of laboratory hydrate formation technique on the loci of hydrate formation at the pore scale and the resulting measured properties.

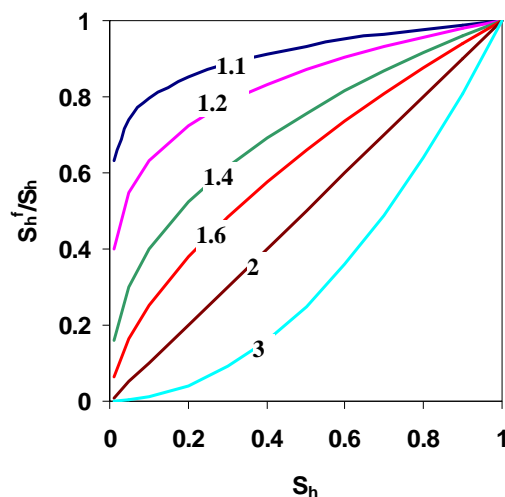


Figure 9. The diagram illustrates the impact of exponential operations on S_h in the mathematical expressions derived to describe our laboratory data. The y-axis shows the ratio between S_h^f and the original value of S_h , where f is the exponent indicated on the curve. For $S_h < 0.2$, power-law relationships profoundly reduce the role of S_h in controlling the trends in physical properties. Even for much higher S_h , the impact of hydrate on sediment properties is still greatly reduced for a range of exponents that emerge from the trends we fit to the data set.

The electrical properties of hydrate-bearing sediments behave largely as bulk medium properties, which implies that S_h is more important than the geochemical interactions between the hydrate and the mineral grains. Thus, the laboratory method used to form hydrate in sediment samples is less important for electrical properties than is carefully controlling S_h and producing a homogeneous sample.

Measured thermal properties might also be expected to reflect the properties of the bulk medium. However, our results indicate that this is not the case. The consequences of grain separation and/or cryogenic suction and lensing during formation of hydrate to high S_h produce thermal conductivity values that cannot be

properly predicted with volume average formulations.

Conversely, both the loci of hydrate formation, which depends on the method used to form hydrate in the laboratory, and soil characteristics play critical roles in controlling large- and small-strain (including seismic velocities) mechanical properties of hydrate-bearing sediments. The trends that emerge from our data clearly reflect the need to capture both factors. Truly isolating the impact of the hydrate formation technique on properties such as strength (Figure 10 of [6]) and seismic velocities (Figure 2) is currently difficult given the different soils and experimental conditions researchers have used to collect such data.

The properties gathered for precipitated silt (with or without hydrate) do not always follow the expected ordering of clay-silt-sand. Thus, the expressions reported here only partially capture the properties of this dual porosity sediment, particularly at $S_h=0.5$. As natural sediments often contain grains with internal porosity and dual porosity pore structures, trends obtained using homogeneous specimens made of solid grains in typical laboratory studies may not always be applicable for predicting the properties of or interpreting physical properties measurements in natural sediments.

This paper focused on the physical properties that are directly measured in the laboratory. Numerous additional parameters can be determined indirectly from the data set. For example, measured seismic velocities can be used to calculate undrained Poisson's ratio and the small-strain shear and bulk moduli. In all cases, the validity of inferred parameters is limited by the applicability of models to the boundary conditions imposed in laboratory tests.

ACKNOWLEDGMENTS

The fundamental data for this study were acquired through the tireless efforts and careful work of numerous students and postdoctoral researchers at Georgia Tech, including F. Francisca, T.S. Yun, J.Y. Lee, D.D. Cortes, and A.I. Martin. From 2002 to 2006, this research was supported by a contract to us at Georgia Tech from the Chevron Joint Industry Project on Methane Hydrates under contract DE-FC26-01NT41330 from the U.S.

Department of Energy. However, any opinions, findings, conclusions, or recommendations expressed herein are those of the authors and do not necessarily reflect the views of the DOE. Additional support was provided by the Goizueta Foundation Chair held by J.C.S. at Georgia Tech. This research was largely completed while C.R. was affiliated with Georgia Tech prior to mid-2006, and we thank D. Hutchinson at the USGS for her continued support of C.R.'s involvement in this research since that time. W. Waite and B. Dugan provided important and timely comments that improved this paper.

REFERENCES

- [1] Santamarina, J.C., Francisca, F., Yun, T.S., Lee, J.Y., Martin, A.I., Ruppel, C. *Mechanical, thermal, and electrical properties of hydrate-bearing sediments*. in *AAPG Hedberg Conference*. 2004.
- [2] Birchwood, R.A., Noeth, S., Tjengdrawira, M. A., Kisra, S. M., Elisabeth, F. L., Sayers, C. M., Singh, R., Hooyman, P. J., Plumb, R. A., Jones, E., Bloys, J. B. *Modeling the mechanical and phase change stability of wellbores drilled in gas hydrates by the Joint Industry Participation Program (JIP) Gas Hydrates Project Phase II*. in *SPE Ann. Tech. Conf.* 2007.
- [3] Ruppel, C., Boswell, R., Jones, E., *Scientific results from Gulf of Mexico gas hydrates Joint Industry Project Leg I drilling: Introduction and overview*. Marine and Petrol. Geol., in press.
- [4] Hutchinson, D.R., D. Shelander, J. Dai, D. McConnell, W. Shedd, M. Frye, C. Ruppel, R. Boswell, E. Jones, T. Collett, K. Rose, B. Dugan, W. Wood, and T. Latham. *Site selection for DOI/JIP gas hydrate drilling in the Northern Gulf of Mexico in International Conference on Gas Hydrates*. 2008. Vancouver, BC, Canada.
- [5] Jones, E., Latham, T., McConnell, D., Frye, M., Hunt, J., Shedd, W., Shelander, D., Boswell, R., Rose, K., Ruppel, C., Hutchinson, D., Collett, T., Dugan, B., Wood, W. *Scientific objectives of the Gulf of Mexico gas hydrate JIP Leg II drilling*. in *Offshore Technology Conference*. 2008.
- [6] Yun, T.S., J.C. Santamarina, and C. Ruppel, *Mechanical properties of sand, silt, and clay containing tetrahydrofuran hydrate*. *Journal of Geophysical Research*, 2007. **112**: p. B04106, doi:10.1029/2006JB004484.
- [7] Yun, T.S., F.M. Francisca, J.C. Santamarina, and C. Ruppel, *Compressional and shear wave velocities in uncemented sediment containing gas*

hydrate. *Geophysical Research Letters*, 2005. **32**: p. L10609, doi:10.1029/2005GL022607.

[8] Lee, J.Y., T.S. Yun, J.C. Santamarina, and C. Ruppel, *Observations related to tetrahydrofuran and methane hydrate for laboratory studies of hydrate-bearing sediments*. *Geochem. Geophys. Geosyst.*, 2007. **8**: p. Q06003.

[9] Lee, J.-Y., *Hydrate-bearing sediments: Formation and geophysical properties*, in *Civil and Environmental Engineering*. 2007, Georgia Institute of Technology: Atlanta. p. 219.

[10] Martin, A.I., *Hydrate-bearing sediments—Thermal Conductivity*, in *School of Civil and Environmental Engineering*. 2005, Georgia Institute of Technology. p. 133 pp.

[11] Buffett, B. and O. Zatssepina, *Formation of gas hydrate from dissolved gas in natural porous media*. *Marine Geology*, 2000. **164**: p. 69-77.

[12] Spangenberg, E., J. Kulenkampff, R. Naumann, and J. Erzinger, *Pore space hydrate formation in a glass bead sample from methane dissolved in water*. *Geophysical Research Letters*, 2005. **32**: p. L24301, doi:10.1029/2005GL024107.

[13] Spangenberg, E. and J. Kulenkampff, *Influence of methane hydrate content on electrical sediment properties*. *Geophysical Research Letters*, 2006. **33**: p. L24315, doi:10.1029/2006GL028188.

[14] Stern, L.A., S.H. Kirby, and W.B. Durham, *Peculiarities of methane clathrate hydrate formation and solid-state deformation, including possible superheating of water ice*. *Science*, 1996. **273**(5283): p. 1843-1848.

[15] Priest, J.A., A. Best, and C.R. Clayton, *A laboratory investigation into the seismic velocities of methane gas hydrate-bearing sand*. *Journal of Geophysical Research*, 2005. **110**: p. B04102, doi:10.1029/2004JB003259.

[16] Winters, W.J., W.F. Waite, D.H. Mason, L.Y. Gilbert, and I.A. Pecher. *Grain size effects on acoustic and strength behavior of sediments containing natural- and laboratory-formed methane gas hydrate*. in *Fifth International Conference on Gas Hydrates*. 2005. Trondheim, Norway.

[17] Berge, L.I., K.A. Jacobsen, and A. Solstad, *Measured acoustic wave velocities of R11 (CCl₃F) hydrate samples with and without sand as a function of hydrate concentration*. *Journal of Geophysical Research*, 1999. **104**(B7): p. 15415-15424.

[18] Fernandez, A. and J.C. Santamarina, *The effect of cementation on the small strain*

parameters of sands. *Canadian Geotechnical Journal*, 2001. **38**(1): p. 191-199.

[19] Santamarina, J.C., K.A. Klein, and M.A. Fam, *Soils and Waves: Particulate materials behavior, characterization and process monitoring*. 2001, New York: John Wiley & Sons, Ltd. 488.

[20] Soga, K., S.L. Lee, M.Y.A. Ng, and A. Klar, *Characterisation and engineering properties of methane hydrate soils*, in *Characterization and Engineering Properties of Natural Soils*, Vol. 4, Tan, T. S., Phoon, K. K., Hight, D. W. & Leroueil, S., Editors. 2006, Taylor and Francis, 2591-2642.

[21] Durham, W.B., L.A. Stern, S.H. Kirby, and S. Circone. *Rheological comparisons and structural imaging of sI and sII endmember gas hydrates and hydrate/sediment aggregates*. in *Fifth International Conference on Gas Hydrates*. 2005: Tapir Academic, Trondheim, Norway.

[22] Jin, Y.K., M.W. Lee, and T.S. Collett, *Relationship of gas hydrate concentration to porosity and reflection amplitude in a research well, Mackenzie Delta, Canada*. *Marine and Petroleum Geology*, 2002. **19**(4): p. 407-415.

[23] Collett, T.S. and J. Ladd, *Detection of gas hydrate with downhole logs and assessment of gas hydrate concentrations (saturations) and gas volumes on the Blake Ridge with electrical resistivity log data*. *Proceedings of the Ocean Drilling Program: Scientific Results*. Vol. 164. 2000. 179-191.